The following publication N. Wang, Z. -L. Sun, Z. Zeng and K. -M. Lam, "Effective Segmentation Approach for Solar Photovoltaic Panels in Uneven Illuminated Color Infrared Images," in IEEE Journal of Photovoltaics, vol. 11, no. 2, pp. 478-484, March 2021 is available at https://doi.org/10.1109/JPHOTOV.2020.3041189.

An Effective Segmentation Approach for Solar Photovoltaic Panels in Uneven Illuminated Color Infrared Images

Nan Wang, Zhan-Li Sun*, *Member, IEEE*, Zhigang Zeng, *Fellow, IEEE*, and Kin-Man Lam, *Senior Member, IEEE*

***Abstract*—How to accurately segment a solar photovoltaic panel in an infrared image is an intractable problem due to some unfavorable factors. In this paper, an effective approach is proposed for solar photovoltaic panel segmentation from infrared images. In order to alleviate the effect of uneven color distribution, a guided filter-based image-enhancement method is first devised to strengthen the edges of solar photovoltaic panels. Moreover, a two-stage method is proposed to detect the contour lines of solar photovoltaic panels. In our algorithm, first, after a thresholding operation, contours in the images are detected by means of a line-segment detector. Then, a method based on *k*-means clustering is employed to eliminate lines caused by noise or unrelated background areas. In addition, a background-subtraction strategy is designed to achieve a more accurate segmentation result by removing the remaining background regions. Experimental results demonstrate the effectiveness and efficiency of the proposed method for the segmentation of solar photovoltaic panels.**

***Index Terms*—Solar photovoltaic panel; image segmentation; image enhancement; straight line detection; *k*-means clustering**

I. Introduction

As a type of clean energy, solar energy can be utilized indefinitely with less geographical restrictions [1], [2]. In recent years, solar photovoltaic panels have been widely used to convert solar energy into electrical energy, due to their relatively low cost [3], [4]. When a photovoltaic cell is inversely polarized or the connector is damaged, the photovoltaic panel will overheat, because all its energy circulates through a small part of the cell [5]. The infrared thermographic imaging provides an effective approach to identify the overheated spots by measuring the superficial temperature of solar photovoltaic panels [6]. Figure 1 shows the acquisition process of infrared images of solar photovoltaic panels, using an unmanned aerial vehicle. For an overheated spot, its pixels' intensities generally exceed twice the mean pixel value of the whole image.

So far, only a few works have been reported for overheated-spot detection for solar panels, by means of infrared thermographic imaging. For overheated-spot detection, one important step is how to accurately segment solar panels from an infrared image. Clustering is a feasible technique for solar panel segmentation, e.g. *k*-means clustering [7], super-pixel clustering [8], etc. Instead of unsupervised clustering, the defect detection was formulated as a classification problem in [9], [10]. In terms of image processing techniques, solar panel segmentation was implemented via line detection or edge detection in [11], [12]. The defect detection can also be carried out via template matching [13] or feature matching [14].

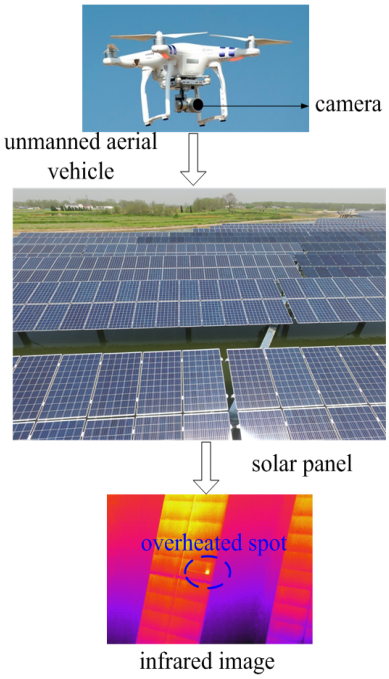

Fig. 1. The acquisition process of infrared images of solar photovoltaic panels, using an unmanned aerial vehicle.

By means of the basis images derived via independent component analysis, the reconstruction error between the test image and its reconstructed image is computed for detecting the presence of defects [15]. In [16], a marker-based watershed transform algorithm was presented to segment solar photovoltaic panels from thermal images. Considering the degree of asymmetry, an enhanced vesselness algorithm was developed for crack segmentation [17]. Nowadays, how to accurately detect the overheated spots is still an intractable task, due to some unfavorable factors, such as noise, uneven color, disturbance of background environment, etc.

Figure 2 shows a comparison of two infrared images with different color distributions. As shown in Fig. 2(a), the whole

Nan Wang and Zhan-Li Sun are with School of Electrical Engineering and Automation, Anhui University, Hefei, China.

Zhigang Zeng is with the School of Artificial Intelligence and Automation, Huazhong University of Science and Technology, Wuhan, China.

Kin-Man Lam is with Department of Electronic and Information Engineering, The Hong Kong Polytechnic University, Hong Kong, China.

*Corresponding author. (e-mail: zhlsun2006@126.com)

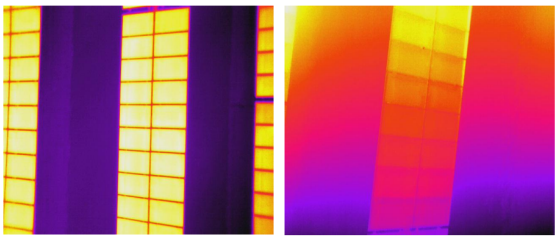

(a) (b)

Fig. 2. A comparison of two infrared images with different color distributions. (a) even illuminated color distribution, (b) uneven illuminated color distribution.

solar panel has distinct boundary lines, and the pixel intensities in each region of a solar panel have small variations. However, we can see from Fig. 2(b) that the pixel intensities increase gradually from the bottom to the top. Moreover, the boundaries of the solar panels become blurred due to the shake of the unmanned aerial vehicle. Because of the uneven illuminated color distribution, it becomes difficult to accurately detect the boundary lines and segment solar panels from infrared images. In this paper, an effective approach is proposed, which combines a guided filter, a line-segment detector (LSD), and a background-subtraction strategy for overheat-spot detection. Experimental results demonstrate the effectiveness and efficiency of the proposed method.

The remainder of the paper is organized as follows. In Section II, we present our proposed algorithm for overheat-spot detection. Experimental results and related discussions are given in Section III, and the concluding remarks are presented in Section IV.

II. Effective Approach for Solar-Panel Segmentation

There are three main components in the proposed method, including the guided filter-based image enhancement, line detection, and background subtraction. A detailed description of these three parts is presented in the following subsections.

A. Guided filter-based image enhancement

For an infrared image $\mathbf{I}$ with three channels (R, G, B), each channel $\mathbf{I}_i$, where i = R, G, or B, is downsampled to reduce the image size. Then, a guidance image $\mathbf{G}_i$ can be obtained by filtering the downsampled image $\mathbf{I}_i$ with a mean filter. Furthermore, the output image $\mathbf{Q}_i$ of the guided filter can be given as a local linear representation of $\mathbf{G}_i$, i.e.,

$$\mathbf{Q}_i = a_k \mathbf{G}_i + b_k, \forall i \in \omega_k, \tag{1}$$

where a_k and b_k are the linear coefficients, and $(\cdot)_i$ denotes the i^{th} pixel in the window ω_k, which is centered at the k^{th} pixel [18].

As a low-pass filter, the guided filter can effectively reduce the noise. However, the edges in $\mathbf{Q}_i$ are blurred at the same time. In order to strengthen the edge information, an enhanced image $\mathbf{A}_i$ is derived by combining $\mathbf{I}_i$ and $\mathbf{Q}_i$, as follows:

$$\mathbf{A}_i = \mathbf{Q}_i + \lambda(\mathbf{I}_i - \mathbf{Q}_i), \tag{2}$$

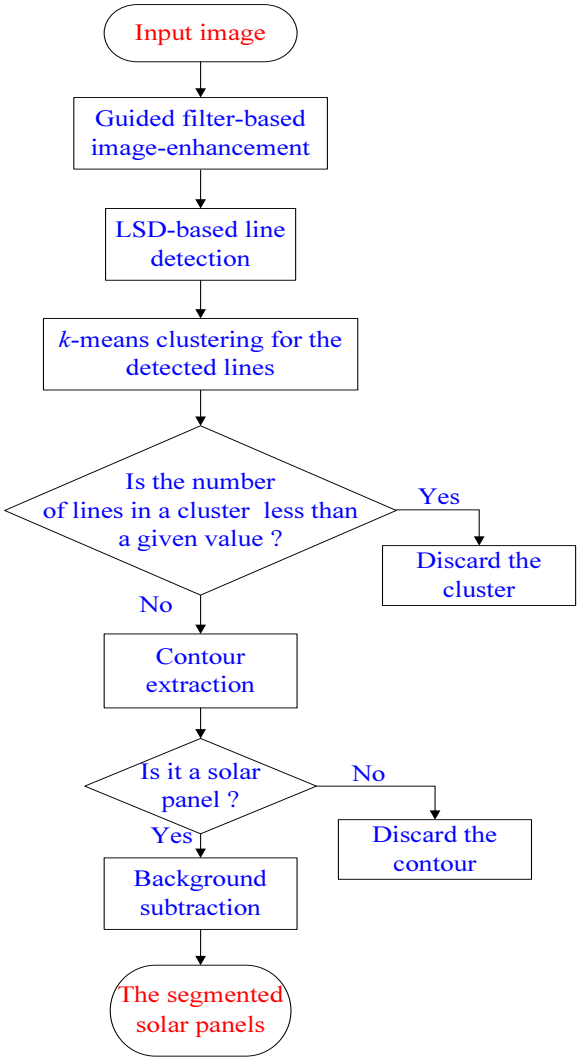

Fig. 3. The flow chart of the proposed method.

where λ is a weighting coefficient.

We can see from (2) that the term $(\mathbf{I}_i - \mathbf{Q}_i)$ corresponds to the edges in the image. Thus, the edges of $\mathbf{Q}_i$ can be strengthened when the weighting coefficient λ is relative large. Nevertheless, as a byproduct, the noise is also added via $\mathbf{I}_i$ at the same time. In order to suppress the noise, the enhanced image $\mathbf{A}$ is first converted into a gray-scale image. Then, a Gaussian filter is applied to the gray-scale image to reduce the noise.

B. Line detection

In general, solar panels have relatively higher pixel intensities than the background regions in an infrared image. Based on this observation, an adaptive threshold operator is applied to every image pixel, according to the neighboring pixels in a sliding window [19]. Furthermore, the Canny edge operator is adopted to detect edges, and the image is converted into a binarization contour image $\mathbf{C}$ [20].

The lines in the contour image are detected via a line segment detector (LSD) [21]. For each pixel $\mathbf{C}(x, y)$ of the contour image, we compute the horizontal gradient $g_x(x, y)$

and the vertical gradient $g_y(x, y)$. Then, the gradient amplitude $g(x, y)$ can be computed as follows:

$$g(x, y) = \sqrt{g_x(x, y)^2 + g_y(x, y)^2}. \quad (3)$$

A pixel is excluded if its gradient magnitude is lower than a given threshold value ρ. Furthermore, the remaining pixels are sorted in the decreasing order, and are divided into the uniform equidistant bins. For the first bin, the pixel with the largest gradient magnitude is selected as the seed. A region starts to grow with a seed, and gradually increases by merging the adjacent pixels.

Define α as the level-line angle of a pixel, which is orthogonal to the gradient angle. The region angle θ_r is initially set as the level-line angle of the seed. At each iteration, θ_r is updated as,

$$\theta_r = \arctan(\frac{\sum_j \sin(\alpha_j)}{\sum_j \cos(\alpha_j)}), \quad (4)$$

where α_j is the level-line angle of the j^{th} adjacent pixel. With a region growing algorithm [21], a line-support region, namely a straight region whose points share roughly the same image gradient angle, is formed by merging the adjacent pixel, whose level-line orientation equals to the region angle up to a certain precision. After this region-growing process, a rectangle with minimum perimeter is constructed, which covers all the pixels in the line-support region.

In order to determine the effectiveness of the line-support region, the number of false alarms (NFA) is defined as follows,

$$NFA(r) = (NM)^{5/2}\gamma \sum_{j=k}^{n} \binom{n}{j} p^j (1-p)^{n-j}, \quad (5)$$

where k is the number of aligned points, p and γ are set as 0.125 and 11, respectively. The parameters N and M are the height and width of the image, respectively. Given a threshold value ε, the line support region is considered to be effective if $NFA < \varepsilon$.

C. Background subtraction

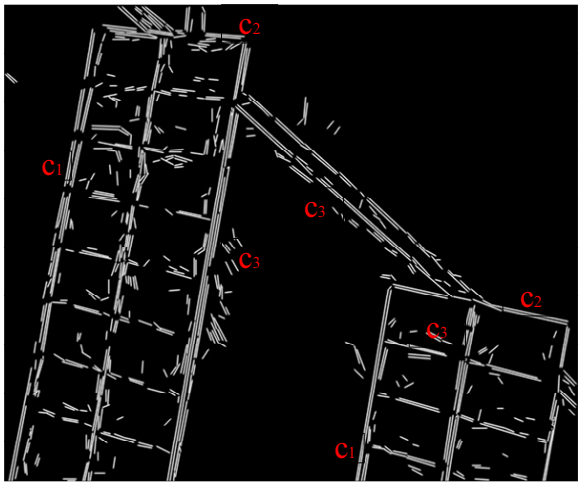

Fig. 4. The three types of lines detected by the LSD algorithm.

Figure 4 shows an example of the lines detected by the LSD algorithm. We can observe that the lines can be divided into three categories, according to their line orientation. The first category (c_1) and the second category (c_2) are those lines with their directions parallel to the long side and the short side, respectively, of the solar panel concerned. The noisy lines and the irrelevant lines in the background belong to the third category (c_3). Moreover, it can be seen that the quantity of the lines belonging to the third category is usually less than that that of the other two categories.

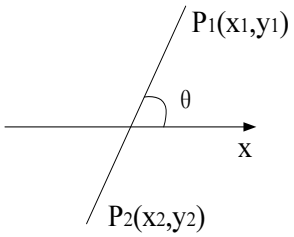

Fig. 5. The angle θ between a detected line (P_2P_1) and the horizontal direction.

As shown in Fig. 5, the orientation of a detected line (P_2P_1) can be denoted as the angle θ between the line and the horizontal line, i.e.

$$\theta = \arctan((y_1 - y_2)/(x_1 - x_2)), \quad (6)$$

where (x_1, y_1) and (x_2, y_2) are the coordinates of the points P_1 and P_2, respectively. Note that the absolute value of θ is less than or equal to $90°$. According to θ, the lines are divided into three categories via the k-means clustering algorithm. Then, the category with the smallest number of lines is discarded in order to remove the noisy and irrelevant lines.

However, we can see from Fig. 4 that the outermost contour of a solar panel is not closed, i.e., the contour is composed of a number of disconnected lines. Thus, a dilation operation is performed to connect these lines by eliminating the discontinuous places [20]. Then, a minimum circumscribed rectangle is constructed to cover the lines. Due to noise, the rectangle still contains some background areas. Thus, a background subtraction is performed so as to more accurately find the areas of solar panels.

Figure 6 shows the background subtraction process, where Fig. 6(a) illustrates the area of the minimum circumscribed rectangle. In order to reduce the background area, we first rotate the rectangle. Given the angle θ of the long side a_1, the rectangle is rotated clockwise by the angle α, which is given as follows:

$$\alpha = \begin{cases} -90 + \theta & \theta \geq 0 \\ 90 + \theta & \theta < 0 \end{cases}. \quad (7)$$

Fig. 6(b) shows the result after rotation. Furthermore, we compute the mean of the pixels in the whole area (μ), as well as the mean for each column (μ_c). If $\mu_c < \mu$, the corresponding column is discarded. After background subtraction, the remaining area is the segmented solar panel.

After segmenting the solar panels, the overheated spots can be detected based on two criteria. The first criterion is

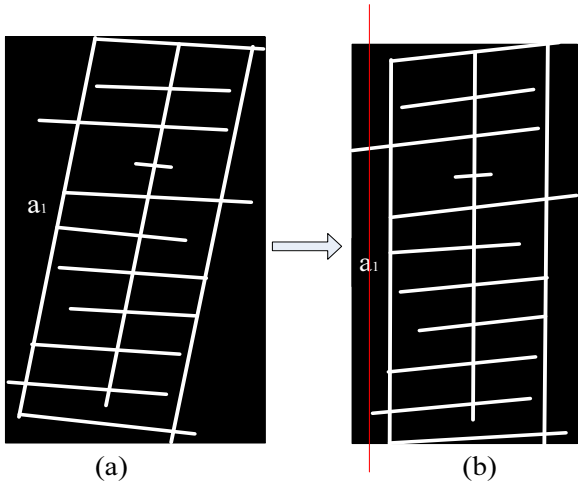

Fig. 6. An example to illustrate the background subtraction operations.

that, for an overheated spot, its pixels' intensities generally exceed twice the mean pixel value of the whole image. Thus, a thresholding operation can be performed to find the possible overheated regions. The second criterion is that the area of an overheated region is far smaller than that of the solar panel. In our proposed method, an overheated region is kept, if its area is less than one thirtieth of the solar panel area. The specific steps of the proposed algorithm are summarized in Algorithm 1.

Algorithm 1 The proposed algorithm.

1: Input: An infrared image $\mathbf{I}$ with three channels (R, G, B), image size: 640×512.
2: *Step 1*: Each channel $\mathbf{I}_i$ is downsampled with a sampling rate of 4.
3: *Step 2*: Compute a_k and b_k according to [18], then obtain $\mathbf{Q}_i$ via (1), where ω_k is set at 5.
4: *Step 3*: Given $\mathbf{I}_i$ and $\mathbf{Q}_i$, compute $\mathbf{A}_i$ by (2), where λ is set at 4.
5: *Step 4*: Obtain the enhanced image $\mathbf{A}$ by merging $\mathbf{A}_i$, then convert $\mathbf{A}$ into a gray-scale image.
6: *Step 5*: Filter the gray-scale image via a Gaussian filter of size 9×9.
7: *Step 6*: Detect edges with the Canny edge detector, in which the low threshold value and the high threshold value are set at 30 and 90, respectively. Then, convert the gray scale image into a binarization contour map.
8: *Step 7*: Detect the lines via the LSD algorithm [21], the parameters are set as follows: $p = 0.125$, $\gamma = 11$.
9: *Step 8*: Compute the angle of a detected line via (6), divide the lines into three categories by the k-means clustering algorithm, and discard the third category.
10: *Step 9*: For the detected lines, perform the dilation operation to eliminate gaps between neighboring lines, with a structuring element of size 7×7.
11: *Step* : Construct the minimum circumscribed rectangle to cover the lines.
12: *Step 10*: Rotate the rectangle via (7), discard the column that the pixel mean is less than that of the whole rectangle.
13: *Step 11*: Search for the overheated spots, such that the pixel intensities generally exceed twice the mean pixel value of the whole image.
14: Output: The locations of the overheated spots.

III. Experimental results

A. Experimental data

The performance of the proposed solar panel segmentation algorithm, denoted as SPS, is evaluated on the data set provided by Hefei Sunwin Intelligence Company Limited. The data set was captured from a photovoltaic station on July 12, 2017. The photovoltaic station, covering an area of about 183,300 square meters, is located at Feidong County, Anhui Province, China. The unmanned aerial vehicle, equipped with a thermal camera from the FLIR Systems Inc., Vue Pro R 640, flied about 14∼16 meters high above the solar photovoltaic panels. For the thermal camera, the resolution is 640×512. In total, there are 565 images in the data set. For each image, the area covered by the solar panel and the overheated location are manually marked to obtain the ground-truth data.

To verify the performance of SPS, we compare it to five other segmentation algorithms, including GrabCut [22], the level set method (LS) [23], the Sparse Field method (SF) [24], the Graph-based image segmentation (Graph) [25], and the saliency detection method (Saliency) [26].

Eight performance metrics, Recall (Re), Specificity (Sp), False positive rate (FPR), False negative rate (FNR), Overall error rate (OER), Precision (Pr), F-Measure (FM), Similarity (Sim), are adopted in our experiments to evaluate the segmentation performance of the various algorithms [27].

B. Experimental comparisons to image segmentation methods

Figure 7 shows an example to illustrate the processed results at different stages of the proposed method. With the original

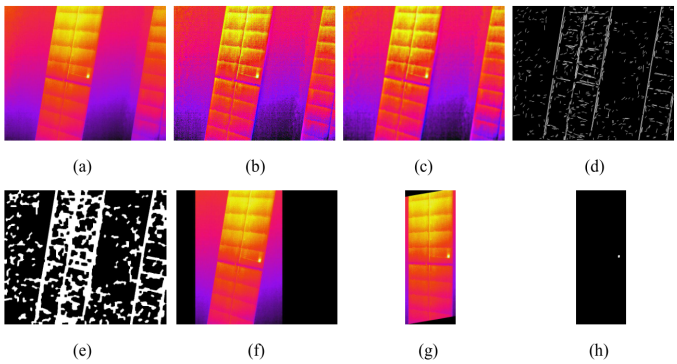

Fig. 7. An example of the processed results at different stages of the proposed method: (a) the original image, (b) the enhanced image, (c) the Gaussian filtering output, (d) LSD, (e) dilation, (f) the initially segmented solar panel, (g) the solar panel after background subtraction, (h) the over-heated spot.

TABLE I
THE PERFORMANCE METRICS OF DIFFERENT SEGMENTATION METHODS.

Methods	Re	Sp	FPR	FNR	OER	Pr	F1	Sim
SPS	**0.977**	0.820	0.180	**0.023**	**11.938**	**0.773**	**0.863**	**0.759**
GrabCut	0.582	0.677	0.323	0.418	35.940	0.530	0.555	0.384
LS	0.423	0.553	0.447	0.577	49.833	0.380	0.400	0.250
SF	0.961	0.809	0.191	0.392	13.247	0.759	0.848	0.736
Graph	0.574	**0.855**	**0.145**	0.426	25.523	0.720	0.639	0.469
Saliency	0.449	0.758	0.242	0.551	36.343	0.546	0.493	0.327

infrared image shown in Fig. 7(a), we can see from Fig. 7(b) that the edges become clearer after the enhancement operation. Nevertheless, compared to Fig. 7(a), more noise appears as shown in Fig. 7(b), because the term $(\mathbf{I}_i - \mathbf{Q}_i)$ in (2) is amplified, which corresponds to the edges and the noise. As shown in Fig. 7(c), the solar panel and the background are smoothed by Gaussian filtering. In Fig. 7(d), it can be seen that the edge lines can be effectively detected by using LSD. However, there are still some lines from the background. Moreover, the contour profile of the solar panel is discontinuous. After the dilation operation, we can see from Fig. 7(e) that the edge lines are enhanced, and the contour profile is closed in representing a solar panel. Compared to the initially segmentation results (Fig. 7(f)), the background areas adjacent to the solar panel are obviously reduced by background subtraction, as shown in Fig. 7(g). Thus, for the segmented solar panels, the use of background subtraction can help reduce the distortion in overheated-spot detection. It can be seen from Fig. 7(h) that the overheated spot is correctly detected from the infrared image.

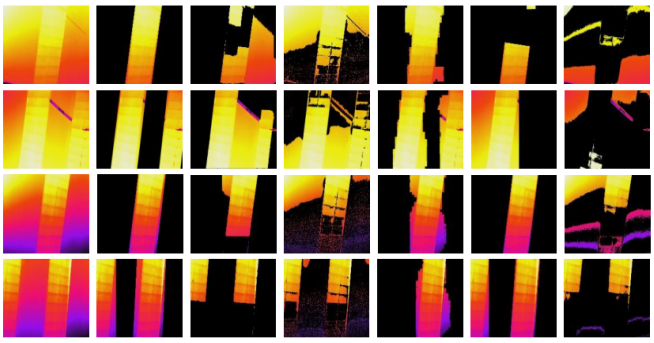

Fig. 8. The solar panel segmentation results of the various algorithms. (a) Original image, (b) SPS, (c) GrabCut, (d) LS, (e) SF, (f) Graph, and (g) Saliency.

As an example, Fig. 8 shows the solar-panel segmentation results based on the various algorithms. The four images shown in Fig. 8(a) a different number of solar panels, background area, noise, and color. Compared to the other methods, the segmentation results based on SPS contain relatively little background noise. Moreover, none of the solar panels is missed in the detection process.

Furthermore, Table I shows the performance metrics of the different segmentation methods. In order to easily compare the performance of the different algorithms, the best results are highlighted in bold. We can see that the proposed method obviously has better performance than the other algorithms.

For the GrabCut method, each pixel is classified as either a foreground or a background pixel via an optimized Gaussian mixture model (GMM). When an infrared image has uneven illuminated color distribution, the GMMs of the foreground and the background are very similar. As a result, the number of misclassified pixels increases significantly, and its performance indices are not as good as SPS. As shown in the fourth row of Fig. 8(c), some foreground pixels were classified as background pixels. Conversely, some background pixels were classified as foreground pixels for the second row of Fig. 8(c).

For the LS method, a contour is derived via the color features. The detected region covered by the contour curve contains some noisy areas, which have similar color to the solar panel. Thus, both the Re and Pr are lower than that of the other methods. For the SF method, a level set contour is evolved from an initial region to capture the variation of the topology structure. When an infrared image has an uneven illuminated color distribution, the segmented region is of irregular shape, which contains some background pixels. Moreover, some foreground pixels are missed, as shown in the fourth row of Fig. 8(e).

The boundary line is indistinct in an infrared image with uneven illuminated color distribution. For the Graph method, region growth may continue to extend for the background or foreground region, due to the vague boundary line. As a result, the performance index Re is low, when some foreground pixels were classified as background pixels, as shown in the first row of Fig. 8(f). On the other hand, the performance index Pre is low, when some background pixels were classified as foreground pixels, as shown in the second row of Fig. 8(f).

The saliency variations of solar panel pixels become larger when the illumination color varies. As a result, for the Saliency method, some regions of the solar panel are missed (the third and fourth rows of Fig. 8(g)), or the solar panel is completely missed (the first and second rows of Fig. 8(g)).

C. Experimental comparisons to solar panel segmentation methods

We also carried out the experiments on three recently reported solar panel segmentation methods, including the Otsu algorithm [28], the grey-level co-occurrence matrix method [29], and the watershed transform algorithm [16]. Compared to the results shown in the papers, the images considered in their experiments were usually captured under good illumination conditions. Due to uneven illuminated color distribution, the performance of these methods is not as good as those previous image segmentation methods. Therefore, we only make a simple analysis of the performances of these methods via some examples.

Figure 9 shows an example of the processed results at different stages for the Otsu algorithm. In the Otsu algorithm, a solar panel is segmented via a thresholding operation. For the grayscale image shown in Fig. 9(c), the pixel intensities of a part of the solar panel are lower than that of the background. As a result, the corresponding region is not detected as solar panel.

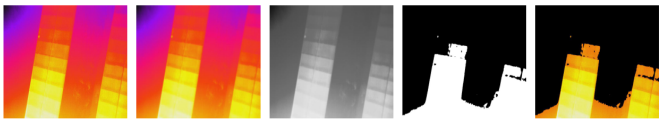

(a) (b) (c) (d) (e)

Fig. 9. An example of the processed results at different stages for the Otsu algorithm: (a) the original image, (b) after Gaussian filtering, (c) the gray-scale image, (d) the binary image obtained via the Otsu algorithm, and (e) the segmented solar panel.

(a) (b) (c) (d) (e)

Fig. 10. An example of the processed results at different stages for the watershed transform algorithm: (a) the original image, (b) the gradient amplitude, (c) the initial segmented result, (d) the contour curve, and (e) the segmented solar panel.

In the watershed transform algorithm, a fixed threshold is used as a segmentation condition. Similar to the Otsu algorithm, some parts of the solar panels are missed in the final segmentation result, as depicted in Fig. 10(e).

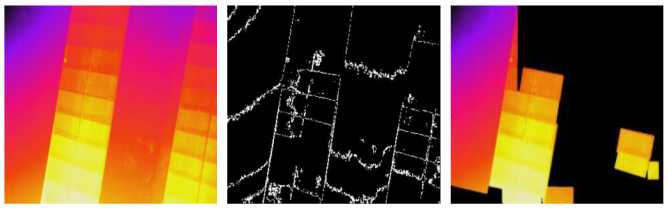

(a) (b) (c)

Fig. 11. An example of the processed results at different stages for the grey-level co-occurrence matrix method. (a) the original image, (b) the initial segmented result, (c) the segmented solar panel.

For the grey-level co-occurrence matrix-based method, the panel's contour is obtained, when the contrast ratio variance is larger than a given threshold value. Nevertheless, the boundary contour can also be detected in the background area with color variation. As a result, some parts of the background are misclassified as solar panel. Meanwhile, some parts of the solar panels failed to be detected, as shown in Fig. 11(c).

D. Related discussions

In order to investigate the effectiveness of our proposed method, Table II shows the experimental comparison of the different enhanced methods, including the guided filter, the dark channel deblurring enhancement method [30], and the retinex enhancement [31]. We can see that the performance is the best, when the guided filter is adopted for image enhancement. For the proposed method, more lines can be detected by using the guided filter. Thus, most contours of a solar panel can be found, and it is seldom for the solar panel to be missed in the detection. Therefore, the performance of SPS is obviously better than those without using enhancement.

TABLE II
THE EXPERIMENTAL COMPARISON OF DIFFERENT ENHANCEMENT METHODS.

Methods	**Re**	**Sp**	**FPR**	**FNR**	**OER**	**Pr**	**F1**	**Sim**
guided filter	**0.977**	0.820	0.180	**0.023**	**11.938**	**0.773**	**0.863**	**0.759**
dark	0.834	0.730	0.270	0.166	23.005	0.659	0.734	0.582
retinex	0.550	**0.832**	**0.168**	0.450	27.644	0.672	0.605	0.434
without	0.827	0.708	0.292	0.173	24.623	0.639	0.721	0.564

TABLE III
THE EXPERIMENTAL COMPARISON WHEN THE k-MEANS CLUSTERING IS USED AND NOT USED IN THE PROPOSED METHOD.

Methods	**Re**	**Sp**	**FPR**	**FNR**	**OER**	**Pr**	**F1**	**Sim**
SPS	**0.977**	**0.820**	**0.180**	**0.023**	**11.938**	**0.773**	**0.863**	**0.759**
without k-means	0.994	0.650	0.350	0.006	21.752	0.640	0.779	0.637

Furthermore, Table III shows the experimental comparison when the k-means clustering is used and not used in the proposed method. For the proposed method, k-means clustering is adopted to eliminate the noisy and irrelevant lines. Nevertheless, some small solar panels may be discarded, due to k-means clustering. Therefore, we can see from Table III that the metric Re is slightly decreased when k-means clustering is used in the proposed method. However, compared to the case without using k-means clustering, the metric Pr is obviously increased, because the background area is reduced by k-means clustering. In addition, it can be seen that the comprehensive performance indices PM and Sim are obviously improved, when k-means clustering is used in the proposed method. Therefore, it is necessary to use k-means clustering to remove noisy and irrelevant lines.

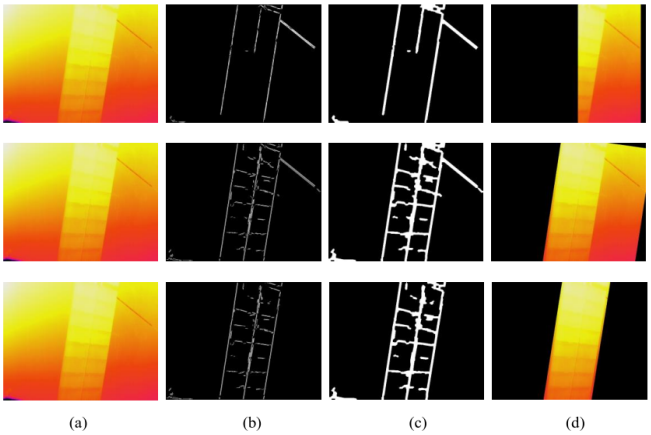

(a) (b) (c) (d)

Fig. 12. The processing results based on three cases, from the first row to the third row to represent the results without enhancement, without k-means clustering, and with both enhancement and k-means clustering: (a) the original image, (b) the lines detected by LSD, (c) the lines after inflation, and (d) the segmented solar panel.

As an example, for the proposed method, Fig. 12 shows the processing results of on three different cases, from the first row to the third row: to represent without enhancement, without k-means clustering, and with both enhancement and k-means clustering. We can see from the first row that the line of the left long side is not detected without the performing enhancement. For the second row, some background areas is are misclassified

TABLE IV
THE RUNTIME (SEC.) PER FRAME OF THE VARIOUS METHODS.

Methods	SPS	GrabCut	LS	SF	Graph	Saliency
runtime	**0.34**	20.43	48.87	61.31	4.31	0.59

as the solar panel, because the unrelated irrelevant lines is are not eliminated, when the k-means clustering is not used in the proposed method. Nevertheless, it can be seen from the third row that the solar panel can be accurately detected, when both the enhancement and the k-means clustering are both adopted in the proposed method.

Table IV shows the runtime (sec.) per frame of the various methods. It can be seen that SPS is more efficient than the other algorithms.

IV. CONCLUSION

In this paper, an effective approach is proposed for solar-panel segmentation from infrared images. The guided filter-based image enhancement has been verified to be able to effectively strengthen edge information. As a result, solar panels can be detected more accurately in the detection process. Moreover, the method based on k-means clustering can effectively remove noisy and irrelevant lines. By means of the background subtraction strategy, the background areas adjacent to a solar panel can be reduced effectively. This can improve the segmentation accuracy. Compared to other state-of-the-art algorithms, the proposed method is more accurate and efficient.

REFERENCES

[1] A. Shekhar, V. K. Kumaravel, S. Klerks, S. Wit, P. Venugopal, N. Narayan, P. Bauer, O. Isabella, and M. Zeman, "Harvesting roadway solar energy-performance of the installed infrastructure integrated PV bike path," *IEEE Journal of Photovoltaics*, vol. 8, no. 4, pp. 1066-1073, 2018.

[2] I. Garcia, W. E. McMahon, M. A. Steiner, J. F. Geisz, A. Habte, and D. J. Friedman, "Optimization of multijunction solar cells through indoor energy yield measurements," *IEEE Journal of Photovoltaics*, vol. 5, no. 1, pp. 438-445, 2015.

[3] I. Celik, A. B. Philips, Z. Song, Y. Yan, R. J. Ellingson, M. J. Heben, and D. Apul, "Energy payback time (EPBT) and energy return on energy invested (EROI) of perovskite tandem photovoltaic solar cells," *IEEE Journal of Photovoltaics*, vol. 8, no. 1, pp. 305-309, 2018.

[4] W. Chen, Y. Duan, L. Guo, Y. Xuan, and X. Yang, "Modeling and prediction of radiated emission from solar cell in a photovoltaic generation system," *IEEE Journal of Photovoltaics*, vol. 6, no. 2, pp. 540-545, 2016.

[5] C. Schuss, K. Leppanen, K. Remes, J. Saarela, T. Fabritius, and B. Eichberger, "Detecting defects in photovoltaic cells and panels and evaluating the impact on output performances", *IEEE Transactions on Instrumentation and Measurement*, vol. 65, no. 5, pp. 1108-1119, 2016.

[6] C. Schuss, K. Remes, K. Leppanen, J. Saarela, T. Fabritius, "Detecting defects in photovoltaic panels with the help of synchronized thermography", *IEEE Transactions on Instrumentation and Measurement*, vol. 67, no. 5, pp. 1178-1186, 2018.

[7] Genevieve C. Ngo and Erees Queen B. Macabebe, "Image segmentation using K-means color quantization and density-based spatial clustering of applications with noise (DBSCAN) for hotspot detection in photovoltaic modules," *IEEE Region 10 Conference*, 2016, pp. 1614-1618.

[8] Moath Alsafasfeh, Ikhlas Abdel-Qader, Bradley Bazuin, "Fault detection in photovoltaic system using SLIC and thermal images," *The 8th International Conference on Information Technology*, 2017, pp. 672-676.

[9] V. S. B. Kurukuru, A. Haque, and M. A. Khan, "Fault classification for photovoltaic modules using thermography and image processing," *IEEE Industry Applications Society Annual Meeting*, 2019, pp. 1-6.

[10] M. Cubukcu and A. Akanalci, "Real-time inspection and determination methods of faults on photovoltaic power systems by thermal imaging in Turkey," *Renewable Energy*, vol. 147, pp. 1231-1238, 2020.

[11] M. Aghaei, A. Gandelli, F. Grimaccia, S. Leva, and R. E. Zich, "IR real-time analyses for PV system monitoring by digital image processing techniques," *International Conference on Event-based Control, Communication, and Signal Processing*, 2015.

[12] M. W. Akram, G. Li, Y. Jin, X. Chen, and A. Ahmad, "Improved outdoor thermography and processing of infrared images for defect detection in PV modules," *Solar Energy*, vol. 19015, pp. 549-560, 2019.

[13] P. Addabbo, A. Angrisano, M. L. Bernardi, G. Gagliarde, A. Mennella, M. Nisi, and S. Ullo, "A UAV infrared measurement approach for defect detection in photovoltaic plants," *IEEE International Workshop on Metrology for AeroSpace*, 2017, pp. 345-350.

[14] X. Li, Q. Yang, Z. Chen, X. Luo, and W. Yan, "Visible defects detection based on UAV-based inspection in large-scale photovoltaic systems," *IET Renewable Power Generation*, vol. 11, no. 10, pp. 1234-1244, 2017.

[15] D. M. Tsai, S. C. Wu and W. Y. Chiu, "Defect detection in solar modules using ICA basis images, " *IEEE Transactions on Industrial Informatics*, vol. 9, no. 1, pp. 122-131, 2013.

[16] A. S. Chaudhary and D. K. Chaturvedi, "Efficient thermal image segmentation for heat visualization in solar panels and batteries using watershed transform", *International Journal of Image Graphics & Signal Processing*, vol. 11, pp. 10-17, 2017.

[17] D. Stromer, A. Vetter, H. C. Oezkan, C. Probst, and A. Maier, "Enhanced crack segmentation (eCS): A reference algorithm for segmenting cracks in multicrystalline silicon solar cells", *IEEE Journal of Photovoltaics*, vol. 9, no. 3, pp. 752-758, 2019.

[18] K. He, J. Sun, "Fast guided filter", *Computer Science*, 2015.

[19] Adrian Kaehler and Gary Bradski, Learning OpenCV 3: Computer Vision in C++ with the OpenCV Library, O'Reilly Media, 2016.

[20] Rafael C. Gonzalez and Richard E. Woods, Digital Image Processing, Publishing House of Electrics Industry, 2017.

[21] R. G. V. Gioi, J. Jakubowicz, J. M. Morel, G. Randall, "LSD: A fast line segment detector with a false detection control", *IEEE Transactions on Pattern Analysis Machine Intelligence*, vol. 32, pp. 722-732, 2010.

[22] P. F. Felzenszwalb, D. P. Huttenlocher, "Efficient graph-based image segmentation", *International Journal of Computer Vision*, vol. 59, pp. 167-181, 2004.

[23] C. Li, R. Huang, Z. Ding, C. Gatenby, D. Metaxas, J. C. Gore, "A level set method for image segmentation in the presence of intensity inhomogeneities with application to MRI", *IEEE Transactions on Image Processing*, vol. 20, pp. 2007-2016, 2011.

[24] S. Lankton, "Sparse field methods-technical report", 2009.

[25] Y. Y. Boykov, M. P. Jolly, "Interactive graph cuts for optimal boundary & region segmentation of objects in N-D images", *IEEE International Conference on Computer Vision*, vol. 1, pp. 105-112, 2001.

[26] M. M. Cheng, G. X. Zhang, N. J. Mitra, X. Huang, S. M. Hu, "Global contrast based salient region detection", *IEEE Conference on Computer Vision and Pattern Recognition*, pp. 409-416, 2011.

[27] Y. Q. Chen, Z. L. Sun, and K. M. Lam, "An effective sub-superpixel-based approach for background subtraction," *IEEE Transactions on Industrial Electronics*, vol. 67, no. 1, pp. 601-609, 2020.

[28] P. Xu, W. J. Zhou, M. R. Fei, "Detection methods for micro-cracked defects of photovoltaic modules based on machine vision", *IEEE International Conference on Cloud Computing and Intelligence Systems*, pp. 609-613, 2014.

[29] S. Salamanca, P. Merchan, I. Garcia, "On the detection of solar panels by image processing techniques", *Mediterranean Conference on Control and Automation*, vol. 3-6, pp. 478-483, July. 2017.

[30] J. Pan, D. Sun, H. Pfister, M. H. Yang, "Blind image deblurring using dark channel prior", *IEEE Conference on Computer Vision and Pattern Recognition*, pp. 1628-1636, 2016.

[31] M. Elad, "Retinex by two bilateral filters", *International Conference on Scale-Space Theories in Computer Vision*, pp. 217-229, 2005.

Nan Wang is now studying in the School of Electrical Engineering and Automation at Anhui University. Her research interests include machine learning, and image and signal processing.

Zhan-Li Sun (M'19) received the Ph.D. degree from the University of Science and Technology of China, in 2005.

Since 2006, he has worked with The Hong Kong Polytechnic University, Nanyang Technological University, and National University of Singapore. He is currently a Professor with School of Electrical Engineering and Automation, Anhui University, China. His research interests include machine learning, and image and signal processing. Dr. Sun serves as an Associate Editor of *IEEE Access*.

Zhigang Zeng (F'20) received the Ph.D. degree in systems analysis and integration from Huazhong University of Science and Technology, Wuhan, China, in 2003.

He is currently a Professor with the School of Automation, Huazhong University of Science and Technology, and also with the Key Laboratory of Image Processing and Intelligent Control of the Education Ministry of China, Wuhan, China. He has authored or coauthored more than 100 international journal papers. His current research interests include theory of functional differential equations and differential equations with discontinuous right-hand sides, and their applications to dynamics of neural networks, memristive systems, and control systems.

Dr. Zeng was an Associate Editor for the IEEE TRANSACTIONS ON NEURAL NETWORKS (2010-2011), and has been an Associate Editor for the IEEE TRANSACTIONS ON CYBERNETICS (since 2014), IEEE TRANSACTIONS ON FUZZY SYSTEMS (since 2016), and a member of the Editorial Board of Neural Networks (since 2012), Cognitive Computation (since 2010), and Applied Soft Computing (since 2013).

Kin-Man Lam (SM'14) received the Associateship in Electronic Engineering with distinction from The Hong Kong Polytechnic University (formerly called Hong Kong Polytechnic) in 1986, the M.Sc. degree in communication engineering from the Department of Electrical Engineering, Imperial College of Science, Technology and Medicine, London, U.K., in 1987, and the Ph.D. degree from the Department of Electrical Engineering, University of Sydney, Sydney, Australia, in August 1996.

From 1990 to 1993, he was a Lecturer at the Department of Electronic Engineering, The Hong Kong Polytechnic University. He joined the Department of Electronic and Information Engineering, The Hong Kong Polytechnic University, as an Assistant Professor in October 1996, became an Associate Professor in 1999, and has been a Professor since 2010. He has been a member of the organizing committee and program committee of many international conferences. Currently, Dr. Lam is a General Co-chair of the IEEE International Conference on Signal Processing, Communications, & Computing (ICSPCC2012). He is a BoG member of the Asia-Pacific Signal and Information Processing Association (APSIPA) and the Director-Student Services of the IEEE Signal Processing Society. Dr. Lam also serves as an Associate Editor of *IEEE Transactions on Image Processing*, *APSIPA Transactions on Signal and Information Processing*, and *EURASIP International Journal on Image and Video Processing*. His current research interests include human face recognition, image and video processing, and computer vision.